Performance of Magnesium Alloy LX41 in a Rat Model

Authors:

Nicole G. Sommer, Sandra Gieringer, Uwe Y. Schwarze, Annelie-M. Weinberg, Talal Al-Samman, Yuri Estrin

Date Submitted: 2023-02-21

Keywords: magnesium-based implants, bioresorbability, in vivo degradation, histology, micro-computed tomography

Abstract:

The biodegradation behavior of a ternary alloy Mg-4Li-1Ca (LX41) was investigated. Preliminary studies of the alloys showed that its property profile may qualify it as a material of choice for bioresorbable bone implants. However, no data on the in vivo behavior of the alloy were available to date. Here we report the results on the in vivo response of juvenile growing rats to implantation over a period of 24 weeks based on micro-computed tomography and histology examination. A comparison with an established Mg-Zn-Ca alloy revealed a higher biodegradation rate of LX41. However, LX41 implants were well integrated, and their faster degradation did not negatively affect bone in-growth and morphology. While lower degradation rates are still desirable, especially at the initial stage of bioresorption, the results obtained suggest that the moderate degradation rates observed will not be detrimental to long-term outcomes of LX41 implantation.

Record Type: Published Article

Submitted To: LAPSE (Living Archive for Process Systems Engineering)

Citation (overall record, always the latest version):	LAPSE:2023.0749
Citation (this specific file, latest version):	LAPSE:2023.0749-1
Citation (this specific file, this version):	LAPSE:2023.0749-1v1

DOI of Published Version: https://doi.org/10.3390/pr10112222

processes

MDPI

Article

In Vivo Performance of Magnesium Alloy LX41 in a Rat Model

Nicole G. Sommer [1,*], Sandra Gieringer [1], Uwe Y. Schwarze [1,2], Annelie-M. Weinberg [1], Talal Al-Samman [3] and Yuri Estrin [4]

[1] Department of Orthopedics and Traumatology, Medical University of Graz, Auenbruggerplatz 5, 8036 Graz, Austria
[2] Division of Oral Surgery and Orthodontics, Department of Dentistry and Oral Health, Medical University of Graz, Billrothgasse 4, 8010 Graz, Austria
[3] Institute for Physical Metallurgy and Materials Physics, RWTH Aachen University, 52056 Aachen, Germany
[4] Department of Materials Science and Engineering, Monash University, Melbourne 3800, Australia
* Correspondence: nicole.sommer@medunigraz.at

Abstract: The biodegradation behavior of a ternary alloy Mg-4Li-1Ca (LX41) was investigated. Preliminary studies of the alloys showed that its property profile may qualify it as a material of choice for bioresorbable bone implants. However, no data on the in vivo behavior of the alloy were available to date. Here we report the results on the in vivo response of juvenile growing rats to implantation over a period of 24 weeks based on micro-computed tomography and histology examination. A comparison with an established Mg-Zn-Ca alloy revealed a higher biodegradation rate of LX41. However, LX41 implants were well integrated, and their faster degradation did not negatively affect bone in-growth and morphology. While lower degradation rates are still desirable, especially at the initial stage of bioresorption, the results obtained suggest that the moderate degradation rates observed will not be detrimental to long-term outcomes of LX41 implantation.

Keywords: magnesium-based implants; bioresorbability; in vivo degradation; histology; micro-computed tomography

Citation: Sommer, N.G.; Gieringer, S.; Schwarze, U.Y.; Weinberg, A.-M.; Al-Samman, T.; Estrin, Y. *In Vivo* Performance of Magnesium Alloy LX41 in a Rat Model. *Processes* **2022**, *10*, 2222. https://doi.org/10.3390/pr10112222

Academic Editor: María Cristina Area

Received: 10 August 2022
Accepted: 4 October 2022
Published: 28 October 2022

1. Introduction

Magnesium (Mg)-based alloys have recently come to the fore in materials engineering as well as preclinical and clinical medical research. They serve as a promising alternative to permanent implant materials (such as stainless steel or titanium-based alloys) in orthopedic and trauma surgery. Their use helps in avoiding stress-shielding effects common to exceedingly stiff permanent implants. A most important advantage of Mg alloys over permanent implant materials is their bioresorbability, which eliminates adverse long-term effects and the need for implant extraction surgery [1,2]. Obviously, the excessively high rate of biodegradation of Mg alloys poses a serious problem hindering their clinical application. Hence, reduction of the degradation rate of Mg alloys without sacrificing their high mechanical strength, is a formidable research target [3,4]. Studies involving several alloying elements have demonstrated improved biodegradation behavior of Mg, including decelerated biocorrosion and suppression of pitting corrosion [5–7]. Alloying of Mg with endogenous elements, such as calcium (Ca) or zinc (Zn), as well as elements used for therapeutic treatments in other clinical settings, has emerged as a preferred strategy, chiefly because of the good mechanical and biodegradation characteristics they enable and the absence of adverse effects [8,9].

Biodegradable Mg-based implants have a long history. It goes back to 1808, when Sir Humphry Davy invented the production of metallic Mg, which formed the basis for the development of biodegradable Mg-based metal implants [10]. The interest in Mg as an implant material reflects its unique combination of properties including excellent bioresorbability, biocompatibility, and suitable mechanical strength comparable to that of

cortical bone [11,12]. The elastic modulus of Mg (41–45 GPa) and its density (1.74 g/cm^3) are similar to those of cortical bone (40–57 GPa and 1.9 g/cm^3, respectively) [7]. Thus, Mg and its alloys offer themselves for clinical applications especially in the field of orthopaedic and trauma surgery.

Although the concept of self-dissolving medical implants is very appealing in theory, its practical execution has met with difficulties. Up to now, the main problem associated with the rapid degradation and the attendant evolution of hydrogen gas bubbles surrounding the implant has not been satisfactorily solved [13].

In the present work, the ternary Mg-based alloy Mg-4Li-1Ca (wt.%), designated as LX41, whose promising properties for biomedical implants had been reported in earlier publications [14–16], was further investigated. It is the presence of Li that, in concert with Ca, had been shown to be responsible for the favourable mechanical properties of the alloy [14–16]. To allay possible concerns about potential toxicity of Li, we should state from the outset that Li has been the gold standard in the treatment of bipolar disorders in psychiatry for decades [17] without major detrimental systemic effects. Recently, the great benefits derived from this chemical element were discovered in entirely different disciplines, e.g., orthopaedics and traumatology [18–23].

In the present study the degradation behaviour of alloy LX41 was investigated in a juvenile growing rat model over a period of 24 weeks by using in vivo low to medium resolution micro-computed tomography (μCT). Results were compared with those for the the established Mg-Zn-Ca alloy ZX00 published earlier [24]. Osseointegration and bone morphology were evaluated after hard-tissue embedding and Levai–Laczko [25] staining of ground samples.

2. Material and Methods

2.1. Material Development and Sterilization

2.1.1. Production of the Material

The investigated Mg alloy LX41 was produced by melting pure Mg (99.95%), Mg-30Ca and Mg-14Li (99.9% Li purity) master alloys in an induction furnace, using a high purity graphite crucible and operating at 500 mbar under a protective atmosphere of Ar and CO_2. The melt was cast into a preheated copper mold coated with a thin layer of BN/Al_2O_3. Subsequent homogenization treatments were conducted at 420 °C for 20 h, after which the homogenized cast billets were air-cooled. The actual chemical composition of the produced alloy (3.98 wt.% Li, 0.98 wt.% Ca, <5 ppm Zr) was verified by means of wet chemical analysis carried out on several specimens from different sites within a homogenized billet.

2.1.2. Thermomechanical Treatment

The thermomechanical treatment chosen was motivated by an earlier study which demonstrated its efficacy regarding the resulting property profile of the alloy [14–16]. Rolling slabs with dimensions of 130 mm × 60 mm × 6 mm were machined from the cast material and annealed at 350 °C for 30 min before rolling [14–16]. The material was then hot rolled at 350 °C with intermediate annealing steps at the same temperature for 10 min. The strain per pass was gradually increased from 0.05 to 0.1. Before the final pass, the rolled material was transferred to another furnace and annealed at 200 °C for 10 min. A much higher strain of 0.27 was employed at the last rolling step in order to refine the microstructure during recrystallisation. After the final pass, the rolled sheet was rapidly quenched in water. Recrystallisation annealing of the rolled sheets was carried out at 350 °C for 30 min. For the current in vivo degradation experiments, rod-shaped specimens (∅ 1.6 mm × 8 mm) were machined from the rolled sheets.

2.1.3. Microstructure and Texture Characterization

Metallographic sample preparation was conducted by mechanical grinding and polishing with 6 μm, 3 μm, 1 μm and 0.25 μm diamond suspension, followed by electrolytic polishing (125 mL C_2H_5OH, 75 mL H_3PO_4) for 45 min. For optical microscopy observations,

the samples were etched with a 10% Nital solution (10% HNO_3 and 90% Ethanol) for 5–6 s and then with Picral solution (10 mL H_2O, 10 mL CH_3COOH, 75 mL 4% picric acid) for 2–3 s. The average grain size of the microstructure in the annealed samples was determined by means of the linear intercept method. The macrotexture evolution of the as-rolled and annealed samples was analysed by X-ray diffraction (XRD), utilizing a texture goniometer D8 Advance (Bruker AXS GmbH, Karlsruhe, Germany) equipped with an area detector. The measurements were carried out with CuKα radiation (λ = 1.5418) at 30 kV and 25 mA. A total of six pole figures, namely $\{10\bar{1}0\}$, {0002}, $\{101\bar{1}\}$, $\{10\bar{1}2\}$, $\{11\bar{2}0\}$ and $\{10\bar{1}3\}$ were recorded and used to calculate the orientation distribution function using the MTEX toolbox [26]. Orientation mappings of the recrystallised LX41 alloy were obtained by means of electron backscatter diffraction (EBSD) attached to a Zeiss LEO1530 field emission gun scanning electron microscope using a step size of 1.3 μm and 70° tilt angle.

2.2. Ethics Statement

Small animal studies were conducted in compliance with the regulations of the Austrian Federal Ministry for Science and Research and the guidelines for accommodation and care of animals as gazetted by the European Convention for the Protection of Vertebrate Animals used for Experimental and Other Scientific Purposes (GZ number: BMWFW66.010/0124-WF/V/3b/2015). All animal experiments in this study followed the 3R principles (replace, reduce, and refine) to minimize suffering of the test animals.

2.3. Animals, Anaesthesia and Analgesia

Four-week-old female Sprague Dawley rats (n = 7) were purchased from Janvier Labs (Saint Berthevin, France) and accommodated on normal chow for the entire study. At six weeks of age, all rats underwent surgery. The cylindrical LX41 implants (l = 8 mm, d = 1.6 mm) were inserted bilaterally, transcortically and proximally into the metaphysis of the tibiae (two implants per rat: 14 implants in total).

For general anaesthesia, volatile isoflurane (Forane®, Abbot AG, Baar, Switzerland) was administered. Beforehand, a subcutaneous combined sedation including Fentanyl (20 μg/kg bodyweight Fentanyl®, Janssen-Cilag GmbH, Neuss, Germany), Midazolam (400 μg/kg bodyweight Midazolam Delta®, DeltaSelect GmbH, Dreieich, Germany) and Medetomidine (200 μg/kg bodyweight Domitor®, Pfizer Corporation Austria GmbH, Vienna, Austria) was administered.

To ensure postoperative analgesia, all Sprague Dawley rats received 200 mg/kg bodyweight Caprofen (Rimadyl, Pfizer Corporation, Vienna, Austria). Caprofen was injected subcutaneously on the day of operation. Analgesia was maintained by administration of 60 mg Piritramid (Dipidolor; Janssen-Cilag GmbH, Neuss, Germany) in 40 mL 5% glucose added to 500 mL drinking water the first postoperative week. Postoperatively, the Sprague Dawley rats were permitted to move unrestrained in their cages with unrestricted weight bearing. Throughout the whole study period daily clinical observation was performed following an accepted protocol [27,28].

2.4. Transcortical Implantation

Preoperative preparation included shaving, disinfection with alcohol pads and drying of both hind legs of a test animals. A 1–2 cm long skin incision was made medially over the proximal lateral tibial metaphysis and the soft tissue was exposed. A bicortical implantation bed was prepared with a 1.55 mm drill with an ascending diameter (Synthes, Paoli, PA, USA). A low rotational speed of 200 rpm was used for drilling. To minimize frictional heat and thermal necrosis, abundant physiological saline irrigation through a syringe was used. Through gentle tapping the cylindrical implant (length of 8 mm, diameter of 1.6 mm) was positioned, resulting in a uniform press fit. Correct transcortical placement was ensured, the operating field was rinsed adequately with physiological saline solution and the wound was stitched up.

Euthanasia was performed twenty-four weeks after transcortical implantation with 25 mg sodium thiopental (Thiopental® Sandoz, Sandoz GmbH, Kundl, Austria) by injection into the cardiac ventricle leading to instantaneous cardiac arrest. All tibiae were excised and fixed in 100% ethanol.

2.5. In Vivo Low to Medium Resolution Micro-Computed Tomography (µCT)

In vivo µCT (Siemens Inveon µCT device) scans were rendered 2, 12, 18 and 24 weeks after surgical implantation at a resolution of 56 µm per voxel. The raw scan data (Supplementary Figure S1a) were converted into DICOM format and imported into the medical image processing software MIMICS (version 23.0, Materialise, Leuven, Belgium). Implant volume, implant surface, and gas volume were assessed via three-dimensional (3D) morphometric analysis. For evaluation, 6–14 pins were used, dependent on the quality of the scan and the respective possibility to properly evaluate all parameters needed.

In brief, each tibia was evaluated individually via the "Image-Reslice Images" function. Image-Reslice Images depicts the implant in all three projections and in all layers. For visualization of the implant, its transversal and longitudinal axes were used as main indicators for editing.

By using the "Segment—New Mask" function, a threshold of 220 to 3071 Hounsfield Units (HU) was placed on the images to separate bone from implant (Supplementary Figure S1b). As the aforementioned Hounsfield Units thresholds did not allow separation of bone and implant in all µCT images, the threshold values had to be adapted individually. Via the "Segment—Split Mask" function, µCT images could be divided in two masks: the rat's bone and the Mg implant (Supplementary Figure S1c). After separation of the two masks, a manual post-processing in all projection planes had to be performed to correct the partially imprecise calculated parts. The correction ensured a precise calculation of implant volume and surface values. A 3D model of the implant was designed via the "Mask—Calculate Part" function and the magnitudes of the volume (in mm^3) and surface (in mm^2) were evaluated.

Another mask was created with "Segment-New Mask", using −879 to −1024 Hounsfield Units, to quantify gas evolution (Supplementary Figure S1d). For precise measurement of the entire gas volume, the threshold values were modified individually. A 3D model of the gas volume was designed via the function "Mask—Calculate Part" and subsequently the gas volume was calculated in mm^3.

2.6. Computation of the Degradation Rate

The degradation rate, DR_i, was determined similarly to previous studies [27]:

$$DR_i = \frac{\Delta V_i}{\overline{S}_i \Delta t} \quad (1)$$

Here i indicates the observation point in time, ΔV_i is the volume change and $\overline{S}_i$ is the average surface area between two consecutive observation points in time within a time interval Δt.

2.7. Qualitative Histological Examination

Using the same procedure as for ZX00 implants [24], tibiae were excised and regions of interest were fixed in 100% ethanol to preserve the tissue and avoid further degradation of LX41 implants. Every three days, ethanol was exchanged to ensure dehydration until infiltration and embedding with Technovit 9100 resin (Kulzer GmbH, Hanau, Germany). The infiltration and embedding process was performed according to the user's manual. Undecalcified thin ground sections of 100 µm were produced according to the Karl Donath method [29]. The sections were stained after Laczko and Levai [25] with azure II, methylene blue and basic fuchsin. Digital images of the thin ground sections were obtained using a custom-made Olympus BX53 scanning system (Olympus Europa SE & Co. KG, Hamburg, Germany).

2.8. Statistical Analysis

As some images of in vivo µCT scans were blurred, not all 14 implants could be investigated, therefore the number of samples was below ten. Nevertheless, all results are still given as mean ± standard deviation (SD) to make them comparable among all groups tested and with literature data. Statistical analysis was performed with GraphPad Prism version 8 (GraphPad Software, San Diego, CA, USA). Differences between the groups and time points were assessed via two-way ANOVA using the Bonferroni's post-hoc test. A p-value < 0.05 was considered statistically significant.

3. Results

3.1. Microstructure

The optical microstructures of the rolled samples (Figure 1a) with and without subsequent annealing are shown in Figure 1b,c, respectively. The as-rolled microstructure comprised large elongated grains in the rolling direction with a significant fraction of deformation twins. Second-phase precipitates were also evident along grain boundaries and in grain interiors (Figure 1b). Upon annealing at 350 °C for 30 min the deformed microstructure was completely recrystallised (Figure 1c) and exhibited equiaxed grain morphology with an average grain size of 18.2 ± 0.6 µm. The grain size distribution of the recrystallised microstructure after annealing is given in Figure 1d. The annealing treatment at 350 °C seemed to have little influence on the shape or distribution of the second-phase precipitates observed in the as-rolled state.

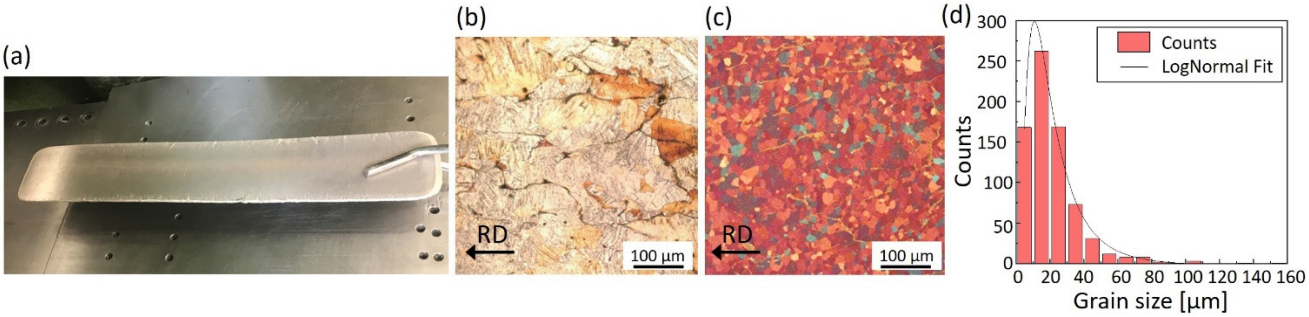

Figure 1. (**a**) LX41 rolled sheet with 65% thickness reduction, (**b**) optical micrograph of the rolling microstructure, (**c**) optical micrograph of microstructure after annealing at 350 °C for 30 min, (**d**) grain size distribution of an as-rolled sample after annealing.

The electron microscopy images in Figure 2 show an example of an annealed specimen illustrating the shape and distribution of precipitates in the recrystallised microstructure. Figure 2a exhibits a region of interest, where a fine distribution of the eutectic Mg_2Ca phase from the as-cast condition is visible (also as a magnified view in Figure 2b). An example of a point scan chemical measurement of the Ca-rich phase by means of energy dispersive spectroscopy (EDS) is given in Figure 2c.

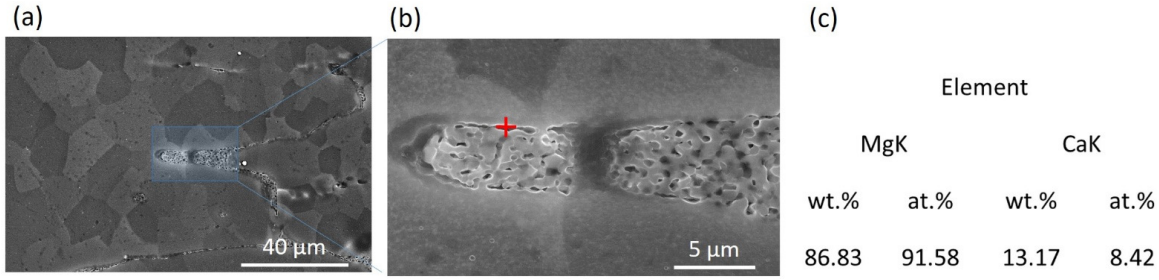

Figure 2. (**a**) Secondary electron image of the annealed microstructure of LX41 alloy, (**b**) magnified image of the area highlighted in (**a**) showing second-phase precipitation, (**c**) energy dispersive X-ray spectroscopy (EDS) results for a representative precipitate in (**b**) identifying a Mg-Ca phase in the Mg matrix. The spot in (**b**) shows an example of an EDX point scan location.

3.2. Texture

Figure 3a shows an EBSD mapping of the 350 °C annealed specimen, reproduced in terms of inverse pole figure (IPF) colouring with respect to the sheet normal direction ND. The poorly defined index white areas in the IPF map are correlated with the second phase precipitates discussed earlier. With respect to the grain size distribution, the microstructure clearly shows two groups of coarse (~70 µm) and fine (<10 µm) recrystallised grains arising from a collective of recrystallisation mechanisms, such as classical nucleation and growth at grain boundaries and triple junctions, and particle-stimulated nucleation. The latter mechanism is known to generate a broad orientation spectrum of the recrystallising nuclei that can weaken the strong basal deformation texture [30–32]. This is in fact seen by the orientation data in Figure 3a, which displays numerous off-basal orientations that seem to have a certain growth advantage during annealing. Additionally, the XRD pole figures in Figure 3b establish a clear texture weakening effect after annealing characterised by a reduction of texture intensity from 8 to 4 mrd (multiples of random distribution).

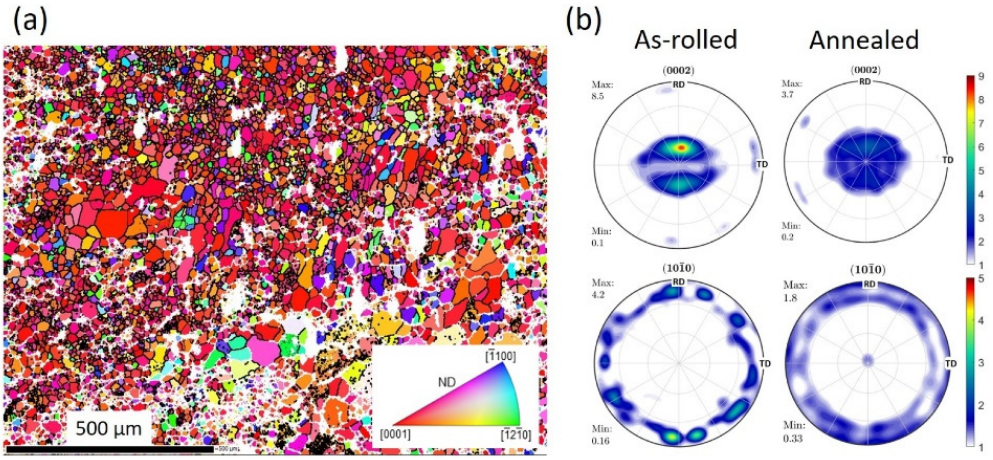

Figure 3. (**a**) Inverse pole figure (IPF) EBSD map with respect to the sheet normal direction (ND) of the annealed LX41 specimen depicting a broad spectrum of crystal orientations, (**b**) XRD textures of the as-rolled and annealed LX41 alloy represented by means of basal and prismatic pole figures. The texture intensity is given in terms of multiples of a random distribution (mrd). The pole figures reveal a significant weakening of the RD-split basal texture evident after rolling deformation.

3.3. Mechanical Behaviour

Figure 4a shows true stress-strain curves in tension at room temperature and constant strain rate of 10^{-3} s^{-1} strain for the as-rolled and the subsequently annealed conditions. As is evident, annealing resulted in a marked increase of ductility in conjunction with a good work hardening capability. At the onset of plasticity, the stress-strain curve of the annealed sample showed a yield plateau at around 86 MPa followed by a work-hardening stage that exhibited a certain level of serrations, likely associated with a Portevin–Le Chatelier (PLC) effect. This effect likely stems from dynamic interactions of moving dislocations with solute atom atmospheres during deformation [33]. It was not investigated further in the current study, but is worth investigating in the future because it may have serious implications regarding plastic instability of the alloy, particularly due to the presence of Ca. The development of Vickers micro-hardness (HV0.1) during annealing is shown in Figure 4b, which clearly exhibits a decrease of hardness from ~62 HV to ~45 HV after 60 min of annealing. The data shows that within the first 6 min of annealing the hardness value decreased slowly. With increasing annealing time, a precipitous drop was observed between 8 min and 10 min, which can be attributed to the onset of recrystallisation after a certain incubation time. After that the hardness remained at a nearly constant level. A summary of the mechanical properties measured in the as-rolled and annealed states is provided in Figure 4c.

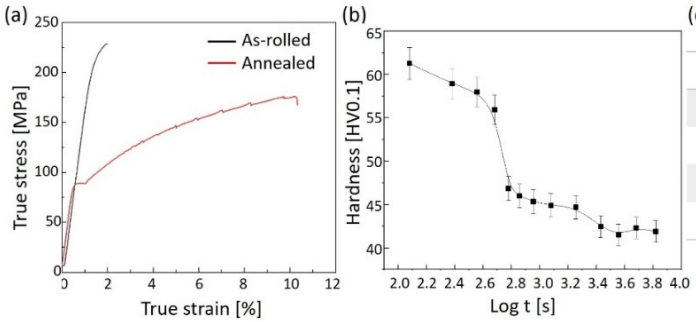

(c)

Properties	As-rolled	Annealed
Yield stress	218 MPa	86 MPa
True UTS	220 MPa	177 MPa
Total elongation	1.7%	11.4%
Micro-hardness	62.34 ± 3.90 HV0.1	44.68 ± 0.95 HV0.1

Figure 4. (**a**) True stress vs. true strain curves for tensile deformation of the as-rolled and the annealed LX41 alloy at ambient temperature for a strain rate of 10^{-3} s^{-1}, (**b**) change of Vickers hardness over the annealing time *t*, (**c**) summary of the mechanical properties for LX41 in the as-rolled and annealed conditions. ('UTS' stands for 'ultimate tensile stress').

3.4. Implant Degradation as Measured by µCT Imaging

For the in vivo study, seven six-week-old Sprague Dawley rats underwent transcortical implantation of cylindrical LX41 pins into the proximal metaphysis of both tibiae. Immediately after surgery (t = 0) as well as 2, 12, 18 and 24 weeks after implantation, low to medium resolution µCT scans were performed (Figure 5a). Data was compared with that from another study in which ZX00 pins with the same dimensions as for the present ZX41 alloy were used [24].

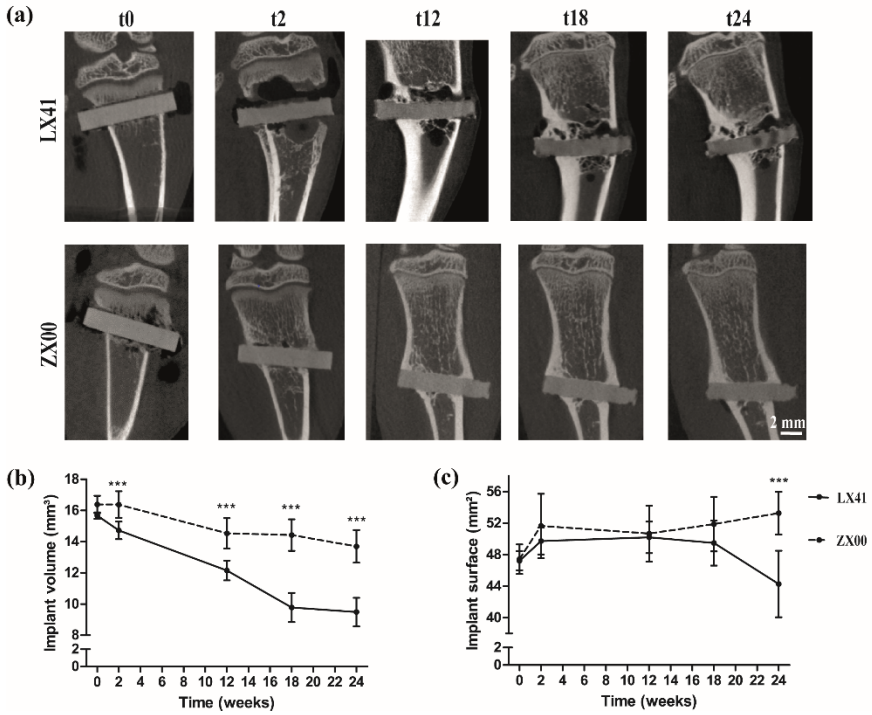

Figure 5. (**a**) In vivo observation of LX41 implant degradation over 24 weeks by µCT imaging. (**b**) Implant volume and (**c**) implant surface area of ZX41 were quantified and compared to ZX00 over a period of 24 weeks (ZX00 reference data published elsewhere [24]). Data in (**b**,**c**) are given as a mean ± SD. *** *p*-value < 0.001.

The measurements of the initial volume of the LX41 pins (t = 0) returned an average value of 15.67 mm^3 ± 0.20 mm^3, whereas the mean volume for ZX00 was initially higher (16.39 mm^3 ± 0.56 mm^3) (Figure 5). LX41 implants showed a continuous decrease in volume over the entire study. Interestingly, there was a significant difference in implant volume between LX41 and ZX00 over the whole test period. After 24 weeks, the mean volume of LX41 implants reached 9.49 mm^3 ± 0.91 mm^3, to be compared with a volume

of 13.93 mm^3 ± 1.27 mm^3 for ZX00. Quantification of the relative implant volume loss revealed a 37.60% decrease for LX41 and a 11.99% decrease for ZX00, respectively [24].

Quantification of the implants' surface area showed that initially the mean values for both alloys were nearly the same: 47.43 mm^2 ± 1.27 mm^2 for LX41 and 47.44 mm^2 ± 1.89 mm^2 for ZX00. Twenty-four weeks after implantation, the surface areas differed significantly, the mean values being 44.53 mm^2 ± 4.22 mm^2 for LX41 and 57.71 mm^2 ± 5.65 mm^2 for ZX00.

We also determined the nominal degradation rate per year defined as the decrement of the implant thickness over the period of testing. The thickness was calculated as the ratio of the mean values of the implant volume and the surface area. The difference between the implant thickness at implantation (t = 0) and 24 days thereafter (in mm per year) was used as the nominal degradation rate. The results revealed a two-fold higher degradation rate for LX41 (0.26 ± 0.06 mm per year) compared to ZX00 (0.12 ± 0.04 mm per year; [24]), which, again, is consistent with the implant volume loss behaviour.

3.5. Increase of the Hydrogen Gas Formation Two Weeks after LX41 Implantation

The evaluation of hydrogen evolution over 24 weeks was performed via in vivo low to medium resolution µCT imaging. Subsequently, 3D reconstruction of LX41 implants and hydrogen gas pockets was performed employing Mimics Software, version 23 (Figure 6a). The volume of hydrogen gas was measured at four different time points (t2, t12, t18, t24 weeks), starting with the first measurement two weeks after surgery. At the starting point t = 0, air inclusions were observed; they were associated with the implantation process and therefore were not counted (Figure 6b). At time point t2 the mean value of the hydrogen gas volume for LX41 was 15.72 mm^3 ± 9.87 mm^3—significantly higher than that for ZX00 implants (2.87 mm^3 ± 3.47 mm^3). At this time point the highest hydrogen gas levels were recorded for both LX41 and ZX00. In the further course of the study, gas evolution gradually subsided, the gas volume reaching an average value of 2.19 mm^3 ± 2.36 mm^3 at the end of the experiment (t24). Similar behaviour was observed for ZX00, with the gas volume attaining an average value as low as 1.58 mm^3 ± 1.53 mm^3 after 24 weeks of implantation [24].

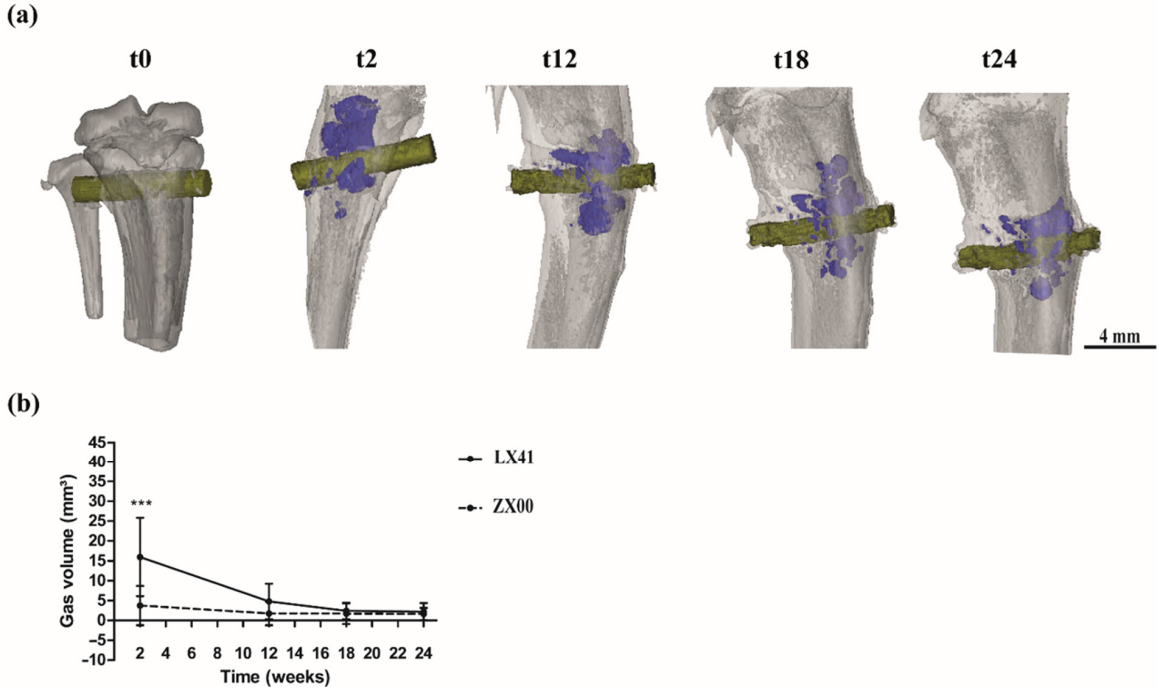

Figure 6. (**a**) For illustrative purposes, one LX41 pin was 3D-reconstructed from the µCT data via Mimics 23.0. at 0, 2, 12, 18 and 24 weeks upon implantation. (**b**) Comparison of hydrogen gas evolution between LX41 and ZX00 over the entire study period of 24 weeks (data for ZX00 adapted from [24]). The volume of hydrogen gas generated by LX41 and ZX00 implants was evaluated 2, 12, 18 and 24 weeks after implantation. The data are shown as a mean ± SD. *** *p*-value < 0.001.

3.6. Histological Evaluation of Osseointegration and Gas Formation for LX41 Pins

To evaluate bone-to-implant contact, bone morphology and any local adverse events caused by LX41 implantation, bones were excised 24 weeks after implantation, dehydrated and embedded in Technovit 9100 New. The region of interest was stained with Levai–Laczko [25] solution (Figure 7). For descriptive histological analysis, three bones with respective implants were used. The overview (Figure 7a,c) showed an intact bone marrow cavity (mc), despite the presence of gas cavities (gc). In the bone tissue area, the pin was almost surrounded by a newly formed bone layer in close contact (green arrow head). The bone layer extended even into the medullary cavity (Figure 7d,f) and was in close contact to the LX41 pin that indicates a good osseointegration. Bone formation still continued as demonstrated in Figure 7f.

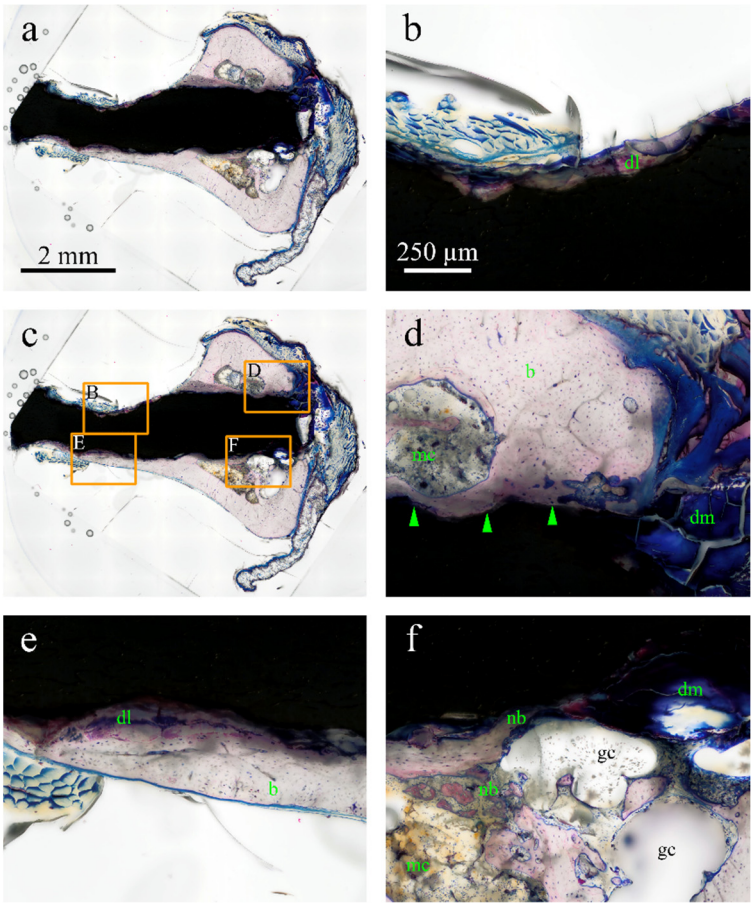

Figure 7. Representative photomicrograph of the proximal metaphysis of the rat tibia 24 weeks after implantation of LX41. (**a**,**c**): overview (scale bar = 2 mm) of the LX41 pin transcortically implanted into the tibia; (**c**): with labeling of the detail regions. (**b**–**f**): magnifications (scale bar = 250 µm) of the respective region of interest indicated by orange rectangles. The pinkish color indicates bone, whereas the blueish color mostly indicates connective tissue. B: in pink going into blue a degradation layer (dl) without any cells or bone in contact. (**d**): medullary cavity (mc) surrounded by bone (b) adjacent to degradation material (dm) in blue, green arrowheads indicate bone in close contact to the implant (**e**): degradation layer (dl) in close contact to bone (b). (**f**): newly formed bone (nb) adjacent to gas cavity (gc) and medullary cavity (mc), degradation material (dm) can also be seen here. Levai–Laczko staining.

The magnification of region of interest (Figure 7f, orange rectangle) highlights new dark pink colored bone (nb) with larger cell nuclei in close proximity to the LX41 pin (nb). The partly visible grey striae were an artefact that occurred when cutting the samples and therefore have no significance for the histological evaluation (orange as-

terisks). Additionally, degradation products were observable at the interface to bone (Figure 7b, dl). Gas bubbles with brown cell detritus were histologically visible adjacent to the pin (Figure 7f, mc). We additionally observed dark blue degradation clods at the tip of the LX41 pin (Figure 7f, dm) and newly formed bone to the LX41 pin (pinkish area; green arrow heads). The light pinkish area further away from the pin contained small cell nuclei indicating older bone (Figure 7d, b).

Figure 7d highlights dark blue crystalline degradation products located at the pin end, which were released and fragmented during the degradation process (dm).

4. Discussion

What is expected of an implant material is an adequate biodegradation rate in bodily fluids. For example, in bone replacement surgery the degradation rate should be commensurate with the rate of bone growth. High enough strength combined with sufficient ductility is a further crucial requirement. Other applications, e.g., in stents, where the demand for high strength is less pressing, call for a different set of properties.

The aim of this study was to assess the degradation rate, gas formation and histological changes seen in the LX41 alloy developed in earlier work. We compared the results of this investigation with those for already more established material ZX00 in terms of the variation of the surface and volume variation of an implant and the concomitant gas evolution [24]. A previous in vitro study by Pan et al. showed that alloying with Li inhibits osteoclastogenesis and proinflammatory cytokine release [20]. It is known that pure Mg has a low corrosion resistance, but it can be enhanced by alloying and thermomechanical processing [10,34–37]. Ca appears to be a favourable alloying element for Mg, as it improves corrosion resistance and promotes good mechanical properties [27,38]. However, a disadvantage of alloying with Ca is the observed loss of formability. In the preliminary material development study by Nene et al. [14], the formability was increased by adding a second alloying element, Li. Lithium promotes ductility and is the most active of the three elements (Mg, Ca, Li) according to the galvanic series of metals. Biocorrosion resistance of alloy LX41 in a simulated body fluid was evaluated, and the performance of the alloy was found to be satisfactory. This improved corrosion resistance was achieved by microstructure refinement using the presence of the harder Mg_2Ca phase acting in concert with the effect of Li and processing by hot rolling. Generally, the microstructure refinement in Mg alloys reduces the propensity for localised corrosion through the formation of a protective layer of $Mg(OH)_2$ since more grain boundary area is then available [14,34,39]. With the average grain size of 5 µm, LX41 is comparable with ZX00 whose grain size was 2–3 µm [40].

The in vivo measurements of the kinetics of biodegradation presented in Section 3.4 and the tensile test results in Section 3.3 give a clear indication that the alloy design specifications for suitability of a material for implant applications can be met by alloy LX41. A comparison of the biodegradation kinetics of alloys LX41 and ZX00 shows a more homogeneous but faster degradation of LX41 after the implantation and throughout the in vivo experiment. ZX00 exhibited an increase in volume at the first two time points (2 and 6 weeks) after implantation [24]. The initial increase is associated with the formation of a layer of corrosion products. According to Witte et al. [41], this newly formed corrosion layer consists mainly of calcium and phosphorus and is a product of the bone-implant interaction and Mg alloy degradation, respectively. Furthermore, they assume that this layer composed of Ca, P, $Mg(OH)_2$ and oxides plays an important role in slowing down the alloy degradation [41]. Although no increase in implant volume was observed for LX41, a homogeneous corrosion layer with degradation clods and reddish areas corresponding to a Ca and phosphate layer was identified by histology.

In comparison with other Mg-based alloys such as ZX50 and WZ21, LX41 performed better in terms of degradation rate. Twelve weeks after implantation, ZX50 was completely dissolved. WZ21 also performed more poorly, with a remaining initial pin volume of approx. 50% after 24 weeks. By contrast, 62.40% initial pin volume was measurable for LX41 after 24 weeks [42]. Indeed, while being twice as rapid as for alloy ZX00, the nominal

rate of LX41 biodegradation, 0.26 ± 0.06 mm per year, compares favourably with that for most Mg-based 'competitors' for bioresorbable implant applications in that it is significantly lower [4]. This moderates the unwanted excessively high rate of hydrogen gas evolution, as was demonstrated in Section 3.5. The mechanical characteristics of LX41 can also be tuned to make the alloy fit for biomedical applications. Thus, the level of the ultimate tensile stress (UTS) of the alloy in the as-rolled condition (220 MPa) exceeds the level required for stents (200 MPa). Annealing necessary to improve elongation to failure and raise it above the 10% mark, as desired in stent implantation, leads to a decrease of UTS down to 177 MPa. This is not dramatic, however, as further thermomechanical processing of the alloy was shown to raise the magnitude of the mechanical characteristics to about 250 MPa for UTS and 23% for tensile elongation [43]. Tunability of the mechanical properties of alloy LX41 by various thermomechanical processing routes provides it with further versatility.

Histologically, LX41 and ZX00 [24] implanted tibiae were comparable with the results obtained by Grün et al. [27]. There were no sclerotic areas or multinucleated giant cells, thereby negating a foreign body reaction occurring in the bone tissue surrounding the implant. In the literature, these reactions have been described mainly in cases of excessively rapid degradation [44,45]. We furthermore detected the formation of new bone tissue around the implant. Despite the more prominent gas development in the case of LX41, the bone marrow cavity appeared to be intact in all areas similarly to ZX00. The formation of a corrosion layer with degradation clods was most pronounced at the pin ends but was also visible along the pin. The occurrence of prominent degradation clods of LX41 was more evident in μCT images, cf. Figure 7, than in the histological images of ZX00, which is probably due to the higher degradation rate of LX41 [27]. Uniform corrosion found in vitro was also shown histologically in our in vivo experiments. However, in addition to the uniform degradation, the present in vivo model also showed several lacunar degradation sites per pin. Despite the good combination of high specific force (142 kN m/kg) and in vitro corrosion resistance, a faster degradation rate than for ZX00 was found [14]. One of the pins showed a very rapid degradation from week 18 onwards. The pin was still present after 24 weeks of implantation but was heavily corroded so that a meaningful evaluation was not possible.

5. Conclusions

The in vivo tests conducted have demonstrated a decreasing degradation rate of LX41 towards the end of the tests, along with a good osseointegration and new bone formation. Based on the findings presented above, we suggest that LX41 does have the potential as a material of choice for the fixation of orthopaedic fractures. To investigate the long-term biodegradation behaviour of LX41 and particularly the beneficial effect of Li, further in-depth studies are necessary. One can expect that the advantages of the use of Li-containing implants in the elderly population will motivate studies of performance of LX41 in osteoporotic conditions.

Supplementary Materials: The following supporting information can be downloaded at: https://www.mdpi.com/article/10.3390/pr10112222/s1, Figure S1: Segmentation of images obtained by in vivo low to medium resolution μCT. In vivo μCT was performed immediately after LX41 implantation (n = 14 pins) as well as 2 (n = 13 pins), 12 (n = 6 pins), 18 (n = 6 pins) and 24 (n = 11 pins) weeks thereafter. (a) The μCT image data underwent segmentation via a grey value orientated region growing algorithm. (b) Bone tissue and the LX41 implants show similar levels of HU. (c) Individual pin and gas evolution segmentation was performed. (d) To quantify gas evolution, a new mask ("Gas mask") was added.

Author Contributions: The authors/co-authors contributed to the manuscript as follows: Conceptualization, N.G.S., T.A.-S. and Y.E.; Methodology, N.G.S., S.G., U.Y.S. and T.A.-S.; Data analysis, N.G.S., S.G., U.Y.S. and T.A.-S.; Writing—Original Draft Preparation, N.G.S., S.G., T.A.-S. and Y.E.; Writing—Review and Editing, N.G.S., U.Y.S., T.A.-S., A.-M.W. and Y.E.; Visualization, N.G.S., T.A.-S., A.-M.W. and Y.E.; Supervision, A.-M.W. and Y.E.; Funding Acquisition, A.-M.W. All authors have read and agreed to the published version of the manuscript.

Funding: This research received no external funding.

Data Availability Statement: The data presented in this study are available on request from the corresponding author. The data are not publicly available due to ethical reasons (animal studies).

Acknowledgments: This work was supported by the Laura Bassi Center of Expertise BRIC (Bioresorbable Implants for Children, FFG–Austria). The authors acknowledge useful discussions with S. S. Nene, B.P. Kashyap and N. Prabhu. T.A.-S. acknowledges the help of Yujun Zhao with the rolling experiments and microstructure characterization. Reference data for ZX00 has been originally published in *Acta Biomaterialia* (see ref. [24]; https://doi.org/10.1016/j.actbio.2022.05.041.). N.S. gives appropriate credit to this original work and its availability under the terms of Creative Commons Attribution License (CC BY; https://creativecommons.org/licenses/by/4.0/).

Conflicts of Interest: The authors declare no conflict of interest.

References

1. Holweg, P.; Herber, V.; Ornig, M.; Hohenberger, G.; Donohue, N.; Puchwein, P.; Leithner, A.; Seibert, F. A lean bioabsorbable magnesium-zinc-calcium alloy ZX00 used for operative treatment of medial malleolus fractures. *Bone Jt. Res.* **2020**, *9*, 477–483. [CrossRef]
2. Herber, V.; Labmayr, V.; Sommer, N.G.; Marek, R.; Wittig, U.; Leithner, A.; Seibert, F.; Holweg, P. Can Hardware Removal be Avoided Using Bioresorbable Mg-Zn-Ca Screws After Medial Malleolar Fracture Fixation? Mid-Term Results of a First-In-Human Study. *Injury* **2022**, *53*, 1283–1288. [CrossRef]
3. Witte, F.; Eliezer, A. Biodegradable Metals. In *Degradation of Implant Materials*; Eliaz, N., Ed.; Springer: New York, NY, USA, 2012; pp. 93–109. [CrossRef]
4. Lin, X.; Saijilafu, X.; Wu, K.; Chen, J.; Tan, L.; Witte, F.; Yang, H.; Mantovani, D.; Zhou, H.; Liang, C.; et al. Biodegradable Mg-based alloys: Biological implications and restorative opportunities. *Int. Mater. Rev.* **2022**, 1–39. [CrossRef]
5. Kirkland, N.T.; Lespagnol, J.; Birbilis, N.; Staiger, M.P. A survey of bio-corrosion rates of magnesium alloys. *Corros. Sci.* **2010**, *52*, 287–291. [CrossRef]
6. Virtanen, S. Biodegradable Mg and Mg alloys: Corrosion and biocompatibility. *Mater. Sci. Eng. B* **2011**, *176*, 1600–1608. [CrossRef]
7. Tsakiris, V.; Tardei, C.; Clicinschi, F.M. Biodegradable Mg alloys for orthopedic implants–A review. *J. Magnes. Alloy.* **2021**, *9*, 1884–1905. [CrossRef]
8. Yu, W.; Chen, D.; Ding, Z.; Qiu, M.; Zhang, Z.; Shen, J.; Zhang, X.; Zhang, S.; He, Y.; Shi, Z. Synergistic effect of a biodegradable Mg–Zn alloy on osteogenic activity and anti-biofilm ability: An in vitro and in vivo study. *RSC Adv.* **2016**, *6*, 45219–45230. [CrossRef]
9. Chen, Y.; Dou, J.; Yu, H.; Chen, C. Degradable magnesium-based alloys for biomedical applications: The role of critical alloying elements. *J. Biomater. Appl.* **2019**, *33*, 1348–1372. [CrossRef]
10. Witte, F. The history of biodegradable magnesium implants: A review. *Acta Biomater.* **2010**, *6*, 1680–1692. [CrossRef]
11. Okuma, T. Magnesium and bone strength. *Nutrition* **2001**, *17*, 679–680. [CrossRef]
12. Kamrani, S.; Fleck, C. Biodegradable magnesium alloys as temporary orthopaedic implants: A review. *Biometals* **2019**, *32*, 185–193. [CrossRef]
13. Kim, Y.K.; Lee, K.B.; Kim, S.Y.; Bode, K.; Jang, Y.S.; Kwon, T.Y.; Jeon, M.H.; Lee, M.H. Gas formation and biological effects of biodegradable magnesium in a preclinical and clinical observation. *Sci. Technol. Adv. Mater.* **2018**, *19*, 324–335. [CrossRef]
14. Nene, S.S.; Kashyap, B.P.; Prabhu, N.; Estrin, Y.; Al-Samman, T. Microstructure refinement and its effect on specific strength and bio-corrosion resistance in ultralight Mg–4Li–1Ca (LC41) alloy by hot rolling. *J. Alloys Compd.* **2014**, *615*, 501–506. [CrossRef]
15. Estrin, Y.; Nene, S.S.; Kashyap, B.P.; Prabhu, N.; Al-Samman, T. New hot rolled Mg-4Li-1Ca alloy: A potential candidate for automotive and biodegradable implant applications. *Mater. Lett.* **2016**, *173*, 252–256. [CrossRef]
16. Nene, S.S.; Estrin, Y.; Kashyap, B.P.; Prabhu, N.; Al-Samman, T.; Luthringer, B.J.; Willumeit, R. Towards microstructure-cytocompatibility relationship in ultralight Mg-4Li-1Ca (LX41) alloy for degradable implant applications. *BioNanoMaterials* **2016**, *17*, 103–111. [CrossRef]
17. McIntyre, R.S.; Berk, M.; Brietzke, E.; Goldstein, B.I.; López-Jaramillo, C.; Kessing, L.V.; Malhi, G.S.; Nierenberg, A.A.; Rosenblat, J.D.; Majeed, A.; et al. Bipolar disorders. *Lancet* **2020**, *396*, 1841–1856. [CrossRef]
18. Zhang, J.; Cai, L.; Tang, L.; Zhang, X.; Yang, L.; Zheng, K.; He, A.; Boccaccini, A.R.; Wei, J.; Zhao, J. Highly dispersed lithium doped mesoporous silica nanospheres regulating adhesion, proliferation, morphology, ALP activity and osteogenesis related gene expressions of BMSCs. *Colloids Surf. B Biointerfaces* **2018**, *170*, 563–571. [CrossRef]
19. Nam, D.; Balasuberamaniam, P.; Milner, K.; Kunz, M.; Vachhani, K.; Kiss, A.; Whyne, C. Lithium for Fracture Treatment (LiFT): A double-blind randomised control trial protocol. *BMJ Open* **2020**, *10*, e031545. [CrossRef]
20. Pan, C.; Chen, L.; Wu, R.; Shan, H.; Zhou, Z.; Lin, Y.; Yu, X.; Yan, L.; Wu, C. Correction: Lithium-containing biomaterials inhibit osteoclastogenesis of macrophages in vitro and osteolysis *in vivo*. *J. Mater. Chem. B* **2019**, *7*, 2566. [CrossRef]
21. Ma, Y.; Li, Y.; Hao, J.; Ma, B.; Di, T.; Dong, H. Evaluation of the degradation, biocompatibility and osteogenesis behavior of lithium-doped calcium polyphosphate for bone tissue engineering. *Bio-Med. Mater. Eng.* **2019**, *30*, 23–36. [CrossRef]

22. Luo, Y.; Li, D.; Zhao, J.; Yang, Z.; Kang, P. In vivo evaluation of porous lithium-doped hydroxyapatite scaffolds for the treatment of bone defect. *Bio-Med. Mater. Eng.* **2018**, *29*, 699–721. [CrossRef]
23. Hu, X.; Wang, Z.; Shi, J.; Guo, X.; Wang, L.; Ping, Z.; Tao, Y.; Yang, H.; Zhou, J.; Xu, Y.; et al. Lithium chloride inhibits titanium particle-induced osteoclastogenesis by inhibiting the NF-κB pathway. *Oncotarget* **2017**, *8*, 83949–83961. [CrossRef]
24. Sommer, N.G.; Hirzberger, D.; Paar, L.; Berger, L.; Ćwieka, H.; Schwarze, U.Y.; Herber, V.; Okutan, B.; Bodey, A.J.; Willumeit-Römer, R.; et al. Implant degradation of low-alloyed Mg–Zn–Ca in osteoporotic, old and juvenile rats. *Acta Biomater.* **2022**, *147*, 427–438. [CrossRef]
25. Lackó, J.; Géza, L. A simple differential staining method for semi-thin sections of ossifying cartilage and bone tissues embedded in epoxy resin. *Mikroskopie* **1975**, *31*, 1–4.
26. Bachmann, F.; Hielscher, R.; Schaeben, H. Texture Analysis with MTEX–Free and Open Source Software Toolbox. *Solid State Phenom.* **2010**, *160*, 63–68. [CrossRef]
27. Grün, N.G.; Holweg, P.; TangI, S.; Eichler, J.; Berger, L.; van den Beucken, J.J.J.P.; Löffler, J.F.; Klestil, T.; Weinberg, A.M. Comparison of a resorbable magnesium implant in small and large growing-animal models. *Acta Biomater.* **2018**, *78*, 378–386. [CrossRef]
28. Kraus, T.; Fischerauer, S.F.; Hänzi, A.C.; Uggowitzer, P.J.; Löffler, J.F.; Weinberg, A.M. Magnesium alloys for temporary implants in osteosynthesis: In vivo studies of their degradation and interaction with bone. *Acta Biomater.* **2012**, *8*, 1230–1238. [CrossRef]
29. Donath, K. *Die Trenn-Dünnschliff-Technik zur Herstellung Histologischer Präparate von Nicht Schneidbaren Geweben und Materialien: Apparate- und Methodenbeschreibung*; EXAKT-Kulzer-Druckschraube: Wehrheim, Germany, 1988.
30. Robson, J.D.; Henry, D.T.; Davis, B. Particle effects on recrystallization in magnesium–manganese alloys: Particle-stimulated nucleation. *Acta Mater.* **2009**, *57*, 2739–2747. [CrossRef]
31. Ball, E.A.; Prangnell, P.B. Tensile-compressive yield asymmetries in high strength wrought magnesium alloys. *Scr. Metall. Et Mater.* **1994**, *31*, 2. [CrossRef]
32. Al-Samman, T. Modification of texture and microstructure of magnesium alloy extrusions by particle-stimulated recrystallization. *Mater. Sci. Eng. A* **2013**, *560*, 561–566. [CrossRef]
33. Kubin, L.P.; Estrin, Y. Evolution of dislocation densities and the critical conditions for the Portevin-Le Châtelier effect. *Acta Metall. Et Mater.* **1990**, *38*, 697–708. [CrossRef]
34. Jin, Y.; Blawert, C.; Yang, H.; Wiese, B.; Feyerabend, F.; Bohlen, J.; Mei, D.; Deng, M.; Campos, M.S.; Scharnagl, N. Microstructure-corrosion behaviour relationship of micro-alloyed Mg-0.5 Zn alloy with the addition of Ca, Sr, Ag, In and Cu. *Mater. Des.* **2020**, *195*, 108980. [CrossRef]
35. Ben-Hamu, G.; Eliezer, D.; Kaya, A.; Na, Y.G.; Shin, K.S. Microstructure and corrosion behavior of Mg–Zn–Ag alloys. *Mater. Sci. Eng. A* **2006**, *435*, 579–587. [CrossRef]
36. Myrissa, A.; Agha, N.A.; Lu, Y.; Martinelli, E.; Eichler, J.; Szakacs, G.; Kleinhans, C.; Willumeit-Römer, R.; Schäfer, U.; Weinberg, A.M. In vitro and in vivo comparison of binary Mg alloys and pure Mg. *Mater. Sci. Eng. C* **2016**, *61*, 865–874. [CrossRef]
37. Zhao, D.; Witte, F.; Lu, F.; Wang, J.; Li, J.; Qin, L. Current status on clinical applications of magnesium-based orthopaedic implants: A review from clinical translational perspective. *Biomaterials* **2017**, *112*, 287–302. [CrossRef]
38. Li, Z.; Gu, X.; Lou, S.; Zheng, Y. The development of binary Mg–Ca alloys for use as biodegradable materials within bone. *Biomaterials* **2008**, *29*, 1329–1344. [CrossRef]
39. Zeng, R.C.; Sun, L.; Zheng, Y.F.; Cui, H.Z.; Han, E.H. Corrosion and characterisation of dual phase Mg–Li–Ca alloy in Hank's solution: The influence of microstructural features. *Corros. Sci.* **2014**, *79*, 69–82. [CrossRef]
40. Brunner, P.; Brumbauer, F.; Steyskal, E.M.; Renk, O.; Weinberg, A.M.; Schroettner, H.; Würschum, R. Influence of high-pressure torsion deformation on the corrosion behaviour of a bioresorbable Mg-based alloy studied by positron annihilation. *Biomater. Sci.* **2019**, *11*, 4099–4109. [CrossRef]
41. Witte, F.; Kaese, V.; Haferkamp, H.; Switzer, E.; Meyer-Lindenberg, A.; Wirth, C.J.; Windhagen, H. In vivo corrosion of four magnesium alloys and the associated bone response. *Biomaterials* **2005**, *26*, 3557–3563. [CrossRef]
42. Kraus, T.; Fischerauer, S.; Treichler, S.; Martinelli, E.; Eichler, J.; Myrissa, A.; Zötsch, S.; Uggowitzer, P.J.; Löffler, J.F.; Weinberg, A.M. The influence of biodegradable magnesium implants on the growth plate. *Acta Biomater.* **2018**, *66*, 109–117. [CrossRef]
43. Tie, D.; Feyerabend, F.; Hort, N.; Hoeche, D.; Kainer, K.U.; Willumeit, R.; Mueller, W.D. In vitro mechanical and corrosion properties of biodegradable Mg–Ag alloys. *Mater. Corros.*. **2014**, *65*, 569–576. [CrossRef]
44. Makkar, P.; Sarkar, S.K.; Padalhin, A.R.; Moon, B.G.; Lee, Y.S.; Lee, B.T. In vitro and in vivo assessment of biomedical Mg–Ca alloys for bone implant applications. *J. Appl. Biomater. Funct. Mater.* **2018**, *16*, 126–136. [CrossRef] [PubMed]
45. Cheng, M.Q.; Wahafu, T.; Jiang, G.F.; Liu, W.; Qiao, Y.Q.; Peng, X.C.; Cheng, T.; Zhang, X.; He, G.; Liu, X. A novel open-porous magnesium scaffold with controllable microstructures and properties for bone regeneration. *Sci. Rep.* **2016**, *6*, 24134. [CrossRef] [PubMed]